

# Recent land deformation detected by Sentinel-1A InSAR data (2016–2020) over Hanoi, Vietnam, and the relationship with groundwater level change

Luyen K. Bui, Phong V. V. Le, Phuong D. Dao, Nguyen Quoc Long, Hai V. Pham, Hong Ha Tran & Lei Xie

To cite this article: Luyen K. Bui, Phong V. V. Le, Phuong D. Dao, Nguyen Quoc Long, Hai V. Pham, Hong Ha Tran & Lei Xie (2021) Recent land deformation detected by Sentinel-1A InSAR data (2016–2020) over Hanoi, Vietnam, and the relationship with groundwater level change, GIScience & Remote Sensing, 58:2, 161-179, DOI: [10.1080/15481603.2020.1868198](https://doi.org/10.1080/15481603.2020.1868198)

To link to this article: <https://doi.org/10.1080/15481603.2020.1868198>



Published online: 01 Feb 2021.



Submit your article to this journal [↗](#)



Article views: 76










View related articles [↗](#)



View Crossmark data [↗](#)



## Recent land deformation detected by Sentinel-1A InSAR data (2016–2020) over Hanoi, Vietnam, and the relationship with groundwater level change

Luyen K. Bui <sup>a</sup>, Phong V. V. Le <sup>b</sup>, Phuong D. Dao <sup>c,d</sup>, Nguyen Quoc Long <sup>a</sup>, Hai V. Pham <sup>e</sup>, Hong Ha Tran <sup>f</sup> and Lei Xie <sup>g</sup>

<sup>a</sup>Faculty of Geomatics and Land Administration, Hanoi University of Mining and Geology, Hanoi, Vietnam; <sup>b</sup>Faculty of Hydrology, Meteorology and Oceanography, VNU University of Science, Vietnam National University, Hanoi, Vietnam; <sup>c</sup>Department of Geography, University of Toronto, Mississauga, Canada; <sup>d</sup>School of the Environment, University of Toronto, Toronto, Canada; <sup>e</sup>INTERA Incorporated, Austin, TX, USA; <sup>f</sup>Faculty of Environment, Hanoi University of Mining and Geology, Hanoi, Vietnam; <sup>g</sup>Department of Land Surveying and Geo-Informatics, Hong Kong Polytechnic University, Hong Kong, China

### ABSTRACT

Interferometric synthetic aperture radar (InSAR), one of the most commonly used remote sensing methods for observing and monitoring land subsidence, has been applied in Hanoi, Vietnam in several studies with results showing deformation up to 2014. However, freely accessible Sentinel-1 InSAR data have not been investigated thoroughly to date. Here, we investigate the most recent land surface deformation in Hanoi for the period 2016 – 2020 using Sentinel-1A SAR data. The analysis is conducted on 114 SAR scenes with both the Persistent Scatterer InSAR (PSInSAR) and Small BAseline Subset (SBAS) methods. The GPS-based deformation time series are used to verify InSAR results and borehole groundwater level measurements are employed to evaluate the relationship between groundwater depletion and surface subsidence. The results show that observed deformation from SBAS and PSInSAR is consistent in both spatial patterns and statistics, in which two high-rate subsiding bowls were detected in Dan Phuong/Hoai Duc and Ha Dong/Thanh Tri districts with the mean subsiding rates of ~5 mm per year. GPS and InSAR deformation generally agree well except for the comparison at the JNAV station after 2017, which can be attributable to the local deformation detected by GPS and the average movement of a 100-m radius area captured by InSAR. An agreement in the drawdown trend between borehole groundwater and InSAR-derived deformation was found at four wells located within or in proximity to the two bowls. The declining rates of groundwater level at about 0.31 m per year were found at the two wells Q57a and Q58a located within the Dan Phuong/Hoai Duc bowl, corresponding to the surface subsidence rates found at 6–8 mm per year. The Q68a well was found to experience groundwater level declining at the highest rate of ~0.9 m per year corresponding to the subsidence rate of ~7 mm per year found by InSAR.

### ARTICLE HISTORY

Received 9 April 2020  
Accepted 13 December 2020

### KEYWORDS

InSAR; Sentinel-1;  
subsidence; groundwater;  
Hanoi; Vietnam

## Introduction

Hanoi city is the capital and the economic, cultural, political, and societal center of the Social Republic of Vietnam. Due to its high population density and rapid urban expansion, there has been a high demand for infrastructure development (Nguyen et al. 2016) and large-scale groundwater exploitation in the region (Saraswat, Kumar, and Mishra 2016; Vu and Tran 2018). These activities have substantially modified the landscape and led to land surface subsidence (Dang et al. 2014). Reinforced by a low-quality municipal sewage and drainage system, land subsidence further exacerbates inundation and causes damage to infrastructures (e.g. Luo et al. 2018; Schramm 2016). Spatio-temporal patterns of surface deformation are

therefore crucial for urban planning to minimize severe influences of surface subsidence.

A number of efforts have focused on detecting and monitoring surface deformation over Hanoi city based on different types of data, e.g. geotechnical, geological, hydrological data (e.g. Nguyen and Helm 1995; Pham et al. 2018; Phi and Strokova 2015; Trinh and Fredlund 2000). These studies often utilized in-situ data of high quality but sparse spatial resolution over limited coverage and discontinuation in time. This fact limits their ability to capture the deformation and its patterns of the surface across space, especially to detect deformation hot spots. Interferometric Synthetic Aperture Radar (InSAR) has demonstrated its ability to capture Earth's surface deformation at

the cm-mm precision with high spatial and temporal resolutions over large-scale areas (Rosen et al. 2000). InSAR has also been applied to retrieve surface deformation over Hanoi using various SAR data, including the Japanese Earth Resources Satellite “FUYO-1” (JERS-1) (1995–1998) (Tran et al. 2007), JERS-1 (1995–1998) and Environmental Satellite Advanced Synthetic Aperture Radar (Envisat-ASAR) (2004) (Nguyen et al. 2017), Advanced Land Observing Satellite Phased Array Type L-Band SAR (ALOS PALSAR) (2007–2011) (Dang et al. 2014), TerraSAR-X (TSX) (2012–2013) (T. S. Le et al. 2016b), TSX and COSMO-SkyMed (CSK) X-band (2011–2014) (Ho et al. 2019), ALOS PALSAR (2007–2011), CSK and TSX (2011–2014) (Tran et al. 2015). However, these studies only show deformation up to 2014, and there is still a general lack of understanding of the most recent deformation trends and patterns in the area.

The European Space Agency (ESA) Sentinel-1 twin missions launched since 2014 have provided free and open data access to the InSAR citizen at a near real-time basis (i.e. within 3 hours of observation). The data have been proved suitable for a wide range of applications, such as marine tracking, ice, and natural disaster monitoring, e.g. landslides or subsidence (Torres et al. 2012). The Sentinel-1 constellation operates at the C-Band frequency with a 12-day repeated acquisition for a single mission (6-day in case of two-satellite combination). The Interferometric Wide-swath (IW) mode of 240 km width is implemented with a high geometric resolution of  $5 \times 20$  m (Yague-Martinez et al. 2016). Though Sentinel-1 data have been widely used to measure surface deformation worldwide associated with, e.g. volcanoes (e.g. Bonforte and Guglielmino 2015; González et al. 2015), earthquake (e.g. Grandin et al. 2016; Lavecchia et al. 2016), water extraction (e.g. Motagh et al. 2017; Sowter et al. 2016), it has not been utilized in Hanoi to date.

In this study, Sentinel-1 SAR data are used for the first time to capture the trends and spatial-temporal patterns of Earth surface deformation in the Hanoi area. The major advancement of Sentinel-1 SAR data is that a significantly larger area will be investigated owing to the IW mode, with a higher and more regular sampling interval. Additionally, this is also the first time InSAR deformation is validated by the GPS-derived deformation time series over Hanoi, and groundwater borehole data are tested for their

consistency with those from InSAR, which present the connection between groundwater exploitation and the surface subsidence. To this end, Sentinel-1 data covering the four-year time span between 3 April 2016 and 13 March 2020, in which the recent surface deformation in the area is missing in the literature, are utilized. Both the Persistent Scatterer InSAR (PSInSAR) and Small Baseline Subset (SBAS) frameworks are implemented for inter-comparison. Although the two methods were proposed with different philosophies, in which PSInSAR is to optimize resolution cells containing a single point scatterer while SBAS aims at optimizing those with distributed scatterers (Hooper et al. 2012), the inter-comparison of deformation detected by both methods is to gain higher confidence of the detected results. In-situ groundwater level time series are adopted to measure the relationship between groundwater withdrawal and surface deformation, and the Global Positioning System (GPS)-based deformation time series is used for testing the consistency between deformation detected by the two techniques, i.e. GPS and InSAR. The data processing is carried out by adopting the InSAR Scientific Computing Environment (ISCE) (Rosen et al. 2012) combined with the Stanford Method for Persistent Scatterer (StaMPS) packages (Hooper et al. 2012) for the PSInSAR approach or the Generic InSAR Analysis Toolbox (GIAnt) packages (Agram et al. 2013) for the SBAS approach.

The paper is structured as follows. Section 2 describes the study area and data adopted, including InSAR, GPS datasets, and groundwater level measurements. The multi-temporal InSAR (MT-InSAR) methods implemented in this study are reviewed in Section 3. Section 4 presents and discusses InSAR-derived deformation results, their validation against the GPS-based deformation time series, and the relationship with borehole groundwater level changes. Finally, Section 5 summarizes the contributions and highlights the significance of the study.

## Study area and datasets

### Study area

The city of Hanoi is located in the northern part of Vietnam. After being merged with parts of Hoa Binh and Vinh Phuc provinces and the entire Ha Tay province in 2008, its geographical location is recently

limited within [ $\sim 20.6^{\circ}\text{N}$ ,  $\sim 21.4^{\circ}\text{N}$ ] in latitude and [ $\sim 105.3^{\circ}\text{E}$ ,  $\sim 106.0^{\circ}\text{E}$ ] in longitude (Figure 1), and covers an area of approximately  $3,359\text{ km}^2$ , which makes it the largest city of Vietnam. It is located in the Vietnamese Red River delta and approximately a hundred kilometers away from the East Sea of Vietnam (see Figure 1). The city is made up of three major types of topography, including delta, midland, and mountainous areas with the average height ranging between three meters and twelve meters, and most of its mountains locating in the North and the West (Tuladhar, Cuong, and Yamazaki 2004).

Hanoi has experienced a rapid construction boom to satisfy housing demand in urbanization, particularly after the expansion, with many skyscrapers built in new urban areas. The speedy urbanization has resulted in a high demand for fresh water for domestic, industrial, and agricultural consumption, which relies mostly on groundwater (Bui et al. 2011). The

rapid construction boom and groundwater over-exploration can result in surface subsidence, which may, in turn, cause severe influences on infrastructure, and makes flooding more serious (Raucoules and Carnec 2000). Here, the study area of  $0.5^{\circ} \times 0.5^{\circ}$  bounded within [ $20.8^{\circ}\text{N}$ ,  $21.3^{\circ}\text{N}$ ] in latitude and [ $105.5^{\circ}\text{E}$ ,  $106.0^{\circ}\text{E}$ ] in longitude, which covers most of the Hanoi area, is investigated (Figure 1).

### Sentinel-1A datasets

In this study, Sentinel-1A data in the Single Look Complex (SLC) format provided in the Copernicus database (Yague-Martinez et al. 2016) are utilized, which can be freely accessed from <https://www.copernicus.eu/en>. We use level-1 data processed in the IW mode, which were acquired in the descending orbit number 91. Sentinel-1B data are available but intermittent and sparse. They are therefore not included in

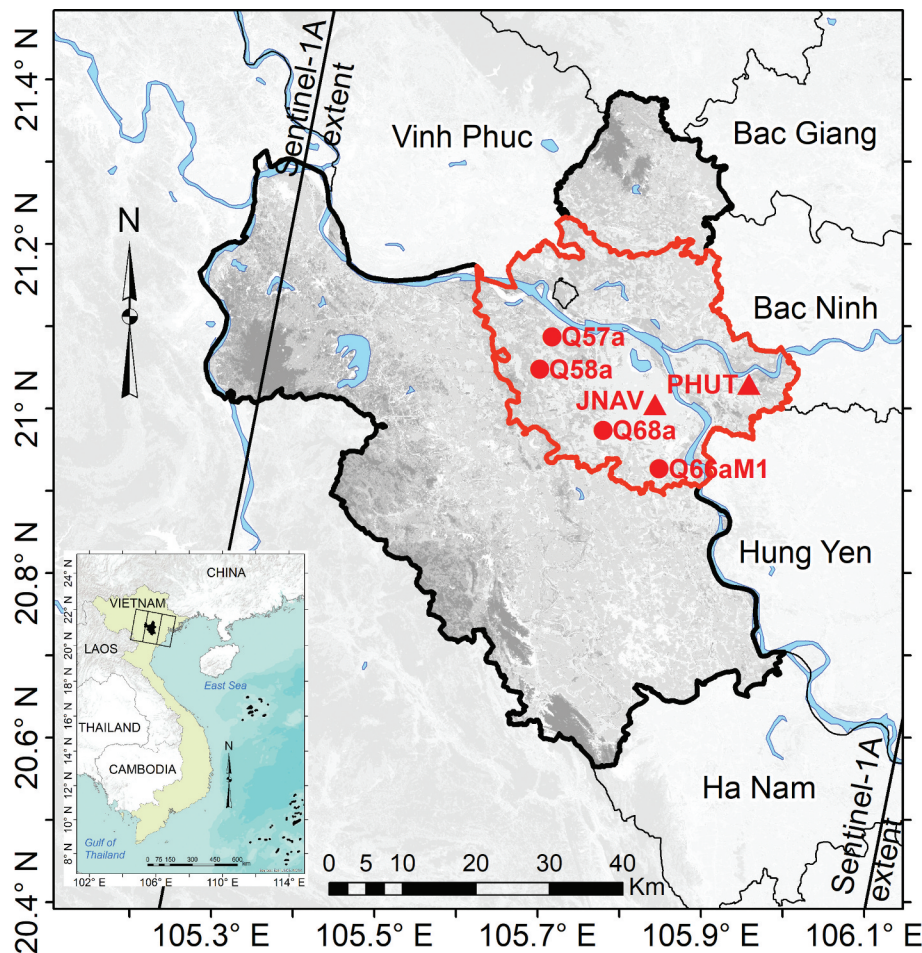


**Figure 1.** Vietnamese mainland map with the city of Hanoi (study area) occupying in the northern part and map of Hanoi with urban districts bounded within the red border. The extent of Sentinel-1A data sub-swaths is indicated by black boxes. Red triangles and dots indicate GPS stations and boreholes used in this study.



the analysis due to their irregular acquisitions. We use 114 Sentinel-1A images covering the 4-year time between 3 April 2016 and 13 March 2020 with a 12-day temporal interval except for some gaps. The radar wavelength of Sentinel-1 is  $\sim 5.55$  cm, which corresponds to the C-band in the microwave spectrum. The main parameters of the used SAR data are listed in Table 1.

Sentinel-1 SLC images are captured by the IW mode adopting Terrain Observation with Progressive Scans SAR (TOPSAR) (De Zan and Guarneri 2006), which are of a 240-km width. Each image comprises three sub-swaths in which the middle one is analyzed in this study, which covers the city of Hanoi (see Figure 1). Each sub-swath involves a series of nine bursts and five of those from the middle sub-swath are included in the analysis as the study area is limited within  $0.5^\circ \times 0.5^\circ$  area. The spatial resolution of Sentinel-1 SLC data is  $5 \times 20$  m.

### GPS and borehole datasets

Two GPS stations available within the study area include JNAV (21.005°N, 105.844°E) and PHUT (21.029°N, 105.959°E) as shown in Figure 1. Both stations are located within urban districts. GPS deformation at the JNAV station is provided by the Nevada Geodetic Laboratory (NGL), which can be freely accessed via <http://geodesy.unr.edu/>, and that at the PHUT station is provided by the Vietnam Academy of Science and Technology (VAST) (M. Le et al. 2016a).

JNAV is an International Global Navigation Satellite System Service (IGS) station of which the data were processed by the GPS Inferred Positioning System (GIPSY) OASIS software package provided by the Jet Propulsion Laboratory (JPL), with the precise point positioning (PPP) method (Hammond, Blewitt, and Kreemer 2016). The velocity of the station is estimated by the Median Interannual Difference Adjusted for

Skewness (MIDAS) (Blewitt et al. 2016) and updated routinely. Two products are provided publicly including five-minute position coordinates updated every hour or every day, and daily position coordinates updated every week (Blewitt, Hammond, and Kreemer 2018). The daily product is adopted in this study.

PHUT is one of the continuously operating GPS stations in Vietnam. The data were collected by a NovAtel GSV4004 receiver and processed by the GAMIT/GLOBK software package, relying on a GPS network connecting with other stations in Vietnam and neighboring countries (Le et al. 2014). The position coordinates at the PHUT station are given in the International Terrestrial Reference Frame 2005 (ITRF2005). The deformation time series from these two stations are used to validate InSAR-derived deformation.

Several boreholes are available throughout the city of Hanoi. The measurements of the hydraulic head at these boreholes were made monthly from 2005 to the end of 2018, which reflects the change in the rates of groundwater exploitation and recharge. In this study, we use borehole groundwater level data observed by the Ministry of Natural Resources and Environment (MONRE), Vietnam. Four monitoring bores with measurements made in the Pleistocene aquifer are exploited in this study including Q57a, Q58a, Q68a, and Q66aM1, which are located in Dan Phuong, Hoai Duc, Ha Dong, and Thanh Tri districts, respectively (Figure 1). These stations are adopted in this study to measure the relationship between Earth surface deformation and the changes in groundwater level as their locations are located within or in close proximity to the areas of high-rate deformation.

## Methods

### InSAR SBAS

#### Interferogram formation

SBAS (e.g. Berardino et al. 2002; Cavalíe et al. 2007; López-Quiroz et al. 2009; Schmidt and Bürgmann 2003; Usai 2003) makes use of a network of multiple interferograms in which temporal and perpendicular baselines are limited in time and length to reduce the effects of decorrelation (e.g. Crosetto et al. 2016; Shanker et al. 2011; Zebker and Villasenor 1992). It is therefore advantageous in that redundant

**Table 1.** Main parameters of the used Sentinel-1 SAR data.

Parameter	Value
Band	C
wavelength	$\sim 5.55$ cm
Orbit number/direction	91/Descending
Sensor mode	IW
Platform	A
Time span	03/04/2016 – 13/03/2020
Temporal interval	12-day
Number of images	114

interferograms are incorporated (Bui, Featherstone, and Filmer 2020). In this study, interferograms are chosen based on the temporal and perpendicular baseline thresholds of 90 days ( $\sim 3$  months) and 200 m, respectively. As a result, 724 interferograms are selected of which the baseline network is depicted in Figure 2(a).

All selected interferograms are subsequently processed in sequence by the ISCE package following the workflows used for processing Sentinel-1 Terrain Observation by Progressive Scans (TOPS) mode image pairs (Fattahi, Agram, and Simons 2017; Rosen et al. 2018; Yague-Martinez et al. 2016). With the study area of  $0.5^\circ \times 0.5^\circ$  bounded within  $[20.8^\circ\text{N}, 21.3^\circ\text{N}]$  in latitude and  $[105.5^\circ\text{W}, 106.0^\circ\text{W}]$  in longitude, five bursts from the central sub-swath are included in the analysis. In the co-registration step, a geometric co-registration is first performed using an external digital elevation model (DEM) and orbit information (Sansosti et al. 2006) on a burst-by-burst basis. Here, the one arc-second Shuttle Radar Topography Mission (SRTM) DEM model (Farr and Kobrick 2000; Smith and Sandwell 2003) and precise orbit information provided by European Space Agency (ESA) are adopted.

With the accuracy requirement of  $\sim 1/1000$  of a pixel in azimuth in the TOPS mode (Fattahi, Agram, and Simons 2017; Yague-Martinez et al. 2016) an enhanced spectral diversity (ESD) approach (Fattahi, Agram, and Simons 2017; Prats-Iraola et al. 2012) is then utilized on subset overlaps to estimate the azimuth misregistration. The ESD is utilized due to its outperformance over cross-correlation techniques (Bamler and Eineder 2005) for Sentinel-1 parameters (Yague-Martinez et al. 2016). The range misregistration is subsequently estimated relying on amplitude correlation over overlap

regions prior to fine offset estimation for full bursts. Finally, burst-by-burst products are merged to derive a stripmap-like product.

The interferograms are then filtered by the Goldstein method (Goldstein and Werner 1998), with the optimal filter strength of 0.4 employed in this study after a number of trials. They are subsequently unwrapped using the statistical-cost network-flow algorithm for phase unwrapping (SNAPHU) (Chen and Zebker 2000) in which the minimum cost flow (MCF) algorithm (e.g. Costantini 1998; Eineder, Hubig, and Milcke 1998; Pepe and Lanari 2006) is applied for initialization. They are finally geocoded to the World Geodetic System 1984 (WGS84) coordinate system and multi-looked with seven range and three azimuth looks.

### Time series analysis

The stack of geocoded interferograms is analyzed by the GInT package (Agram et al. 2013) following the SBAS processing chain documented in Agram, Jolivet, and Simons (2012). A coherence threshold of 0.2 is used to select coherent pixels in such a way that only pixels with coherence larger than this threshold in all interferograms are considered as coherent and are included in the SBAS analysis. Here, without evidence of a stable area, i.e. the area with almost no deformation, the deformation of coherent pixels is computed with respect to the mean deformation of the study area.

Differential atmospheric delay in the interferometric phase, which is correlated with the topography, is reduced using the ERA-Interim Re-Analysis products provided in European Center for Medium-Range Weather Forecast (ECMWF) repository following steps documented in Doin et al. (2009) and Jolivet et al. (2011). The network deramping is then applied

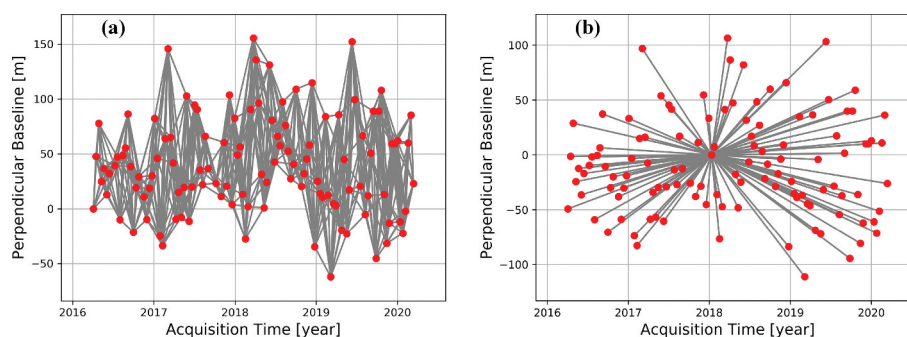


**Figure 2.** Baseline plots of interferograms used in SBAS (a) and PSInSAR (b). The interferograms used in SBAS are chosen based on the temporal and perpendicular baseline thresholds of 90 days and 200 m, respectively, whilst those used in PSInSAR are selected with 11/01/2018 being the primary (formerly master) image. Red dots represent SAR scenes and gray lines indicate interferograms selected.

to atmospheric-corrected interferograms to reduce orbital errors (i.e. ramps) (Biggs et al. 2007; Cavalié et al. 2008; Jolivet et al. 2012; Lin et al. 2010).

After interferograms are reduced for atmospheric and orbital errors, the SBAS approach (e.g. Berardino et al. 2002; Cavalié et al. 2007; López-Quiroz et al. 2009; Schmidt and Bürgmann 2003; Usai 2003) is applied to coherent pixels to invert interferometric phase measurements to the deformation time series. This is carried out on a pixel-by-pixel basis applying the singular value decomposition (SVD) algorithm. The uncertainties are, at the same time, estimated for coherent pixels at all acquisitions applying a Jackknife test. A SBAS rate map is then created by fitting a linear function to the SBAS-derived deformation time series of coherent pixels.

### **PSInSAR**

PSInSAR is another frequently used MT-InSAR method, which is optimized for resolution cells consisting of a single point scatterer (e.g. Colesanti et al. 2003; Ferretti, Prati, and Rocca 2001; Hooper et al. 2004; Lyons and Sandwell 2003; Werner et al. 2003). It, therefore, has an ability to associate Earth's surface deformation with a dominant scatterer, which is smaller than the entire pixel (Hooper et al. 2012). In PSInSAR, all interferograms are generated with respect to a single primary (formerly master) image, which allows for a reduction of the noise contribution of the primary image as it exists in all interferograms.

The ISCE package is again applied to produce a stack of co-registered SLCs. In this step, the same workflow as that implemented in Section 3.1 is employed. The one arc-second SRTM DEM and precise orbit information are used first for a geometric co-registration followed by a refined azimuth co-registration, which is implemented by a Network-based ESD (NESD) approach (Fattahi, Agram, and Simons 2017). All SAR images are cropped to the  $0.5^\circ \times 0.5^\circ$  study area, which comprises five bursts included in the central sub-swath before they are co-registered with respect to the first one (i.e. 03/04/2016).

The PSInSAR method is then applied to the stack of co-registered SLCs using the StaMPS package (Hooper et al. 2012), in which 11/01/2018 is selected as the

primary date to minimize the overall perpendicular and temporal baselines (see Figure 2(b)). PS pixels defined by their phase stability are first selected by a two-step procedure. For computation efficiency, the amplitude dispersion with a threshold of 0.4 is adopted to select an initial subset of PS pixels, i.e. PS candidates. The mean phase computed from surrounding candidates is then subtracted from each PS candidate. The residual phase component caused by DEM error is then computed in the least squares sense and removed. The temporal coherence is subsequently estimated to select the final PS pixels based on a threshold computed by their probability density function (PDF) with an aim at maximizing the number of real selected pixels. This procedure is carried out iteratively three times where, in each iteration, the mean phase is re-calculated after eliminating candidates with low temporal coherence prior to re-calculation of temporal coherence for all candidates (for a detailed description of the workflow and equations used in this PS pixel selection, readers are referred to Hooper et al. (2004)).

The selected PS pixels are then reduced for spatially uncorrelated DEM error as mentioned above. The remaining components include phase change due to Earth's surface deformation and residual error and noise sources, i.e. atmospheric artifacts, orbital error, noise term, and residual error due to inaccuracy in this DEM error correction involving spatially correlated part. The spatially uncorrelated DEM corrected phase is then unwrapped utilizing the three-dimension method with two dimensions in space and one dimension in time (Hooper and Zebker 2007). After unwrapping, the remaining error and noise sources of which the spatially correlated parts are assumed to be uncorrelated in time are reduced (Hooper et al. 2004). The unwrapped phase is therefore high-pass filtered in time then low-pass filtered in space to derive phase change due to surface deformation. A PSInSAR rate map is then created by fitting a linear function to the derived deformation time series of coherent scatterers. Figure 3 compares the simplified flowcharts of steps of SBAS and PSInSAR applied in this study. The top blocks indicate the interferogram formation in SBAS and the generation of co-registered SLC stack in PSInSAR, both are processed by ISCE. The bottom blocks show the time series analysis according to the two methods.

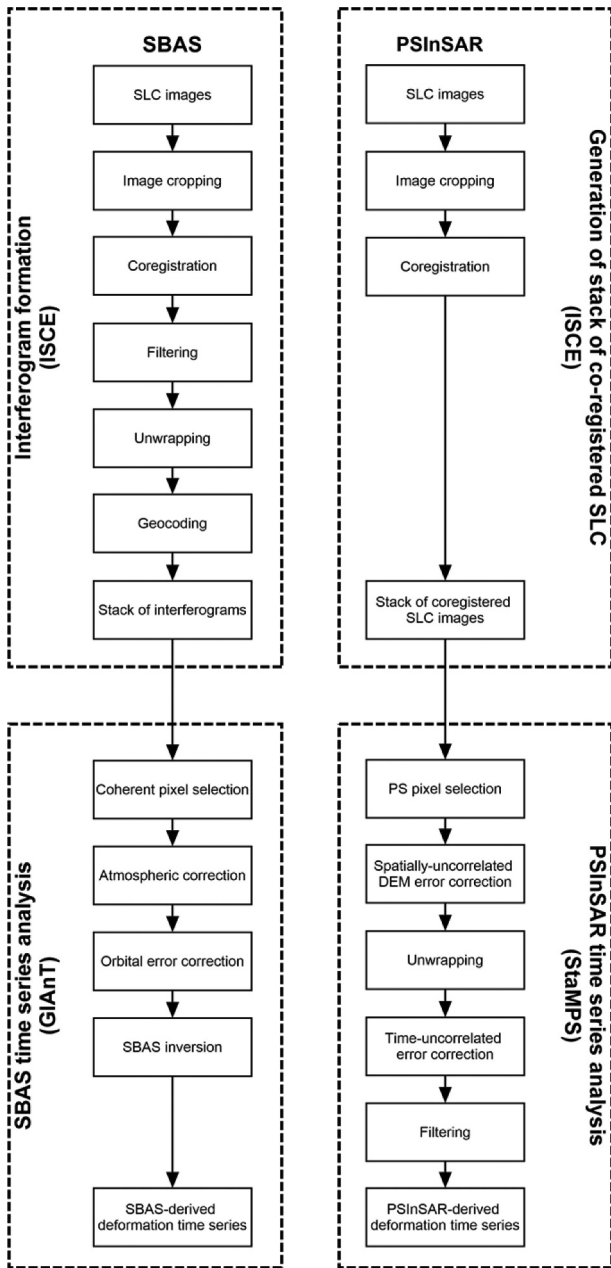


**Figure 3.** Flowcharts of SBAS and PSInSAR data processing applied in this study.

### Stacking

In this study, the stacking method is adopted to obtain the deformation rate map, which is then compared with those derived from SBAS and PSInSAR. Stacking is a simple method where the average of the linear deformation rate is computed which is also referred to as the “average” method (Hetland et al. 2012). This method can be applied to increase the signal-to-noise ratio (SNR) if surface deformation is a single quickly occurred event or a gradual

movement with a constant deformation rate (Simons and Rosen 2015). Averaging multiple interferograms can also reduce tropospheric errors if they are assumed to be random (Lyons and Sandwell 2003), because the neutral atmosphere, which is mainly confined to the troposphere, is uncorrelated at time spans longer than one day (Emardson, Simons, and Webb 2003).

As the number of observations is reduced by utilizing the stacking method, the computational burden in parameter estimation is reduced (Pritchard, Ji, and Simons 2006). The measured displacement of a pixel in the  $i^{\text{th}}$  interferogram can be written as (Emardson, Simons, and Webb 2003; Simons and Rosen 2015):

$$\rho_i = \vartheta T_i + \varepsilon_i \quad 1$$

where  $\rho_i$ ,  $T_i$ , and  $\varepsilon_i$  are the corrected range change, the time separation between primary and secondary (formerly slave) images and the measurement error corresponding to this  $i^{\text{th}}$  interferogram, respectively,  $\vartheta$  is the constant rate of the considered pixel.

The above equation can be re-written as a linear system of all interferograms as:

$$d = \theta \vartheta + E \quad 2$$

where,  $d$ ,  $\theta$  and  $E$  are the vectors of interferogram displacements, time spans, and errors, respectively.

By applying the least squares principle, the deformation rate can be estimated as:

$$\vartheta = (\theta^T W \theta)^{-1} \theta^T W d \quad 3$$

where  $W$  is the weight matrix, which is the inverse of the full data covariance matrix.

## Results and discussion

### Map of deformation rates

To have an overview of the spatial patterns of surface deformation over the entire study area, maps of deformation rates at coherent pixels/scatterers are generated frequently. We first produce a deformation rate map relying on corrected interferograms corresponding to the SBAS network in Figure 2(a) applying the stacking method described in Section 3.3, of which the results are shown in Figure 4(a). A SBAS rate map is then created by fitting a linear function to the SBAS-



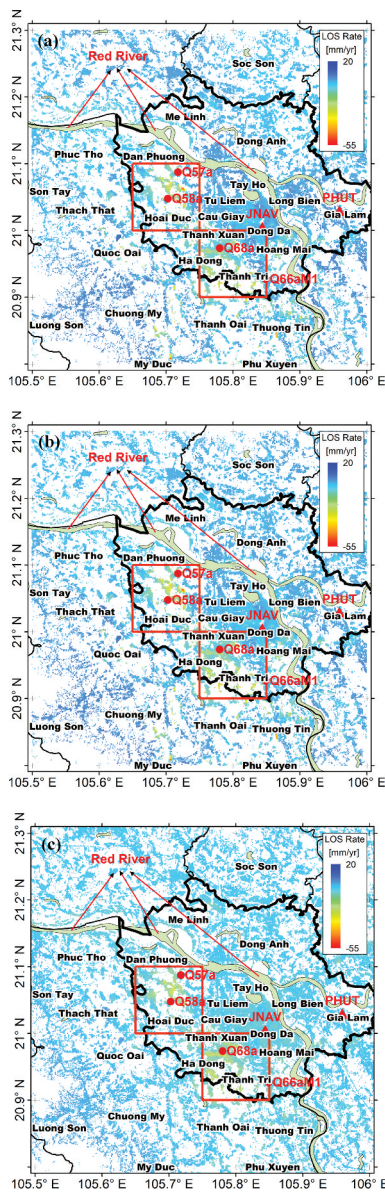


**Figure 4.** Maps of deformation rates in the line of sight direction from Sentinel-1A data covering the 4-year time between 3 April 2016 and 13 March 2020: (a) from the stacking method, (b, c) derived by fitting a linear regression to the SBAS and PSInSAR-derived deformation time series, respectively. Red squares mark two subsiding bowls at high deformation rates in Dan Phuong/Hoai Duc and Ha Dong/Thanh Tri. Red triangles and dots indicate GPS stations and boreholes used in this study.

derived deformation time series of coherent pixels as described in Section 3.1, which is shown in Figure 4(b). This is then applied to PSInSAR coherent scatterers to produce a PSInSAR rate map, which is depicted in Figure 4(c).

The annual rate maps shown in Figure 4 conventionally indicate that positive and negative values represent the surface movement toward (i.e. uplift) and away from (i.e. subsidence) the SAR satellite, respectively. An agreement in the spatial patterns estimated from stacking, SBAS, and PSInSAR is found in Figure 4, which shows subsidence at high rates occurring in two bowls, Dan Phuong/Hoai Duc and Ha Dong/Thanh Tri, which are situated to the south of the Red River (see red squares in Figure 4).

Table 2 compares this study with those in the literature in terms of data used, time span, spatial coverage, and methods applied. The studies are of different spatial coverages depending on data availability and the objectives. Previous studies have smaller study areas due to their Stripmap mode compared to the wide swath mode used in this study. This indicates the improvement of the study in capturing surface deformation and its patterns in a significantly wider area compared to previous studies, which only focused on the deformation hot spots. Other main differences are time acquisition, time span, and the number of scenes used, which proves the renovation of this study in both longer study time and higher sampling interval indicated implicitly by the number of SAR scenes used (see Table 2).

The consistency in the spatial distribution of deformation rates can be found between this study and existing ones. Generally, ground stability appears to the northern part of Red River (Dang et al. 2014), whilst in the southern part, deformation

**Table 2.** Comparison of this study and studies in the literature. The bracketed numbers refer to the number of SAR scenes used.

Reference	SAR Data	Time span	Spatial coverage (km <sup>2</sup> )	Processing method
Tran et al. (2007)	JERS-1 (3)	8/1995 – 9/1998	~400	Three-pass DInSAR
Dang et al. (2014)	ALOS (22)	2/2007 – 2/2011	~1300	PSInSAR
T. S. Le et al. (2016b)	TSX (23)	4/2012 – 11/2013	~30	SBAS
Ho et al. (2019)	TSX (19) CSK (27)	5/2011 – 12/2014	~200	PSInSAR
This study	Sentinel-1 (114)	4/2016 – 3/2020	~3000	SBAS PSInSAR

at higher rates of centimeters order can be found, particularly in new urban districts (Dang et al. 2014; T. S. Le et al. 2016b) (see Figure 4 also). Particularly, previously detected subsiding bowls in Hoai Duc-Tu Liem (Dang et al. 2014) and Ha Dong-Thanh Xuan (Dang et al. 2014; Ho et al. 2019; Le et al. 2016b) are coincident with the Dan Phuong/Hoai Duc and Ha Dong/Thanh Tri bowls, respectively, found in this study, even though the results were retrieved from different SAR missions and at different time spans, i.e. Sentinel-1 and 4/2016–3/2020 here, ALOS PALSAR and 2/2007–2/2011 in Dang et al. (2014), TSX/CSK and 5/2011–12/2014 in Ho et al. (2019), and TSX and 4/2012–11/2013 in T. S. Le et al. (2016b).

In comparison between stacking and SBAS, very similar results have been retrieved with maximum subsidence found being  $-53.3$  mm per year (herein mm/yr) and  $-50.6$  mm/yr, respectively. Other statistics including maximum, minimum, mean, and standard deviation of deformation rates estimated from the two methods are almost equivalent, which are listed in Table 3. The estimated rates at coherent pixels from the two methods are therefore considered identical, which are demonstrated via their histograms with normal density distribution fit as shown in Figure 5(a,b). This is reasonable due to that the two methods are applied to the same coherent pixels with the same interferogram set according to the SBAS network in Figure 2(a). Additionally, the

deformation time series are processed following the same workflow by the ISCE package as described in Section 3.1, but they follow different algorithms to estimate annual rates, i.e. stacking and linear fit to the SBAS deformation time series.

Despite significantly different maximum subsidence estimated from SBAS ( $-50.6$  mm/yr) and PSInSAR ( $-28.2$  mm/yr), their distributions of annual rates in terms of histograms are relatively comparable as depicted in Figure 5(b, c). This can also be demonstrated through their statistics of annual rates shown in Table 3, including maximum, minimum, mean, and standard deviation, which are fairly close between the two methods. Indeed, 99.89% of SBAS-derived rates fall within the range of PSInSAR-derived rates, which are bounded between  $-28.2$  mm/yr and  $+13.2$  mm/yr (see Table 3).

We note that SBAS and PSInSAR are distinct MT-InSAR algorithms as described in Sections 3.1 and 3.2, which are applied to different coherent pixels/scatterers adopting different interferogram sets shown in Figure 2 (cf. left and right panels). However, their results are fairly identical in both terms of spatial patterns of deformation rates (Figure 4) and their statistics (Table 3). In the following Sections, the SBAS- and PSInSAR-derived deformation time series will be validated against GPS-derived deformation and tested their relationship with groundwater level changes.

We then characterize land motions over the two subsiding bowls. A preliminary center point is first identified for each bowl then annual rates of a  $0.1 \times 0.1$ -degree area corresponding to  $\sim 11 \times 11$  km are extracted as a representative of the bowl. Figure 6 shows maps of deformation rates zoomed in to the two subsiding zones derived from stacking, SBAS, and PSInSAR. The estimated

**Table 3.** Statistics of annual rates derived from stacking, SBAS, and PSInSAR. Units in mm/yr.

Statistics	Stacking	SBAS	PSInSAR
Maximum	+ 18.5	+ 18.8	+ 13.2
Minimum	- 53.3	- 50.6	- 28.2
Mean	+ 1.4	+ 1.2	+ 0.1
Standard deviation	4.5	4.6	3.2

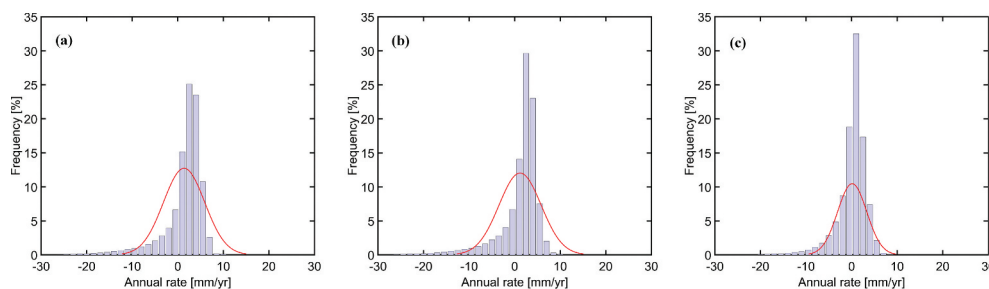


**Figure 5.** Histograms showing frequencies of annual rates at coherent pixels/scatterers computed with equal bins: (a) stacking, (b) SBAS, (c) PSInSAR. A normal density function is fit to the histograms with results shown by red curves.

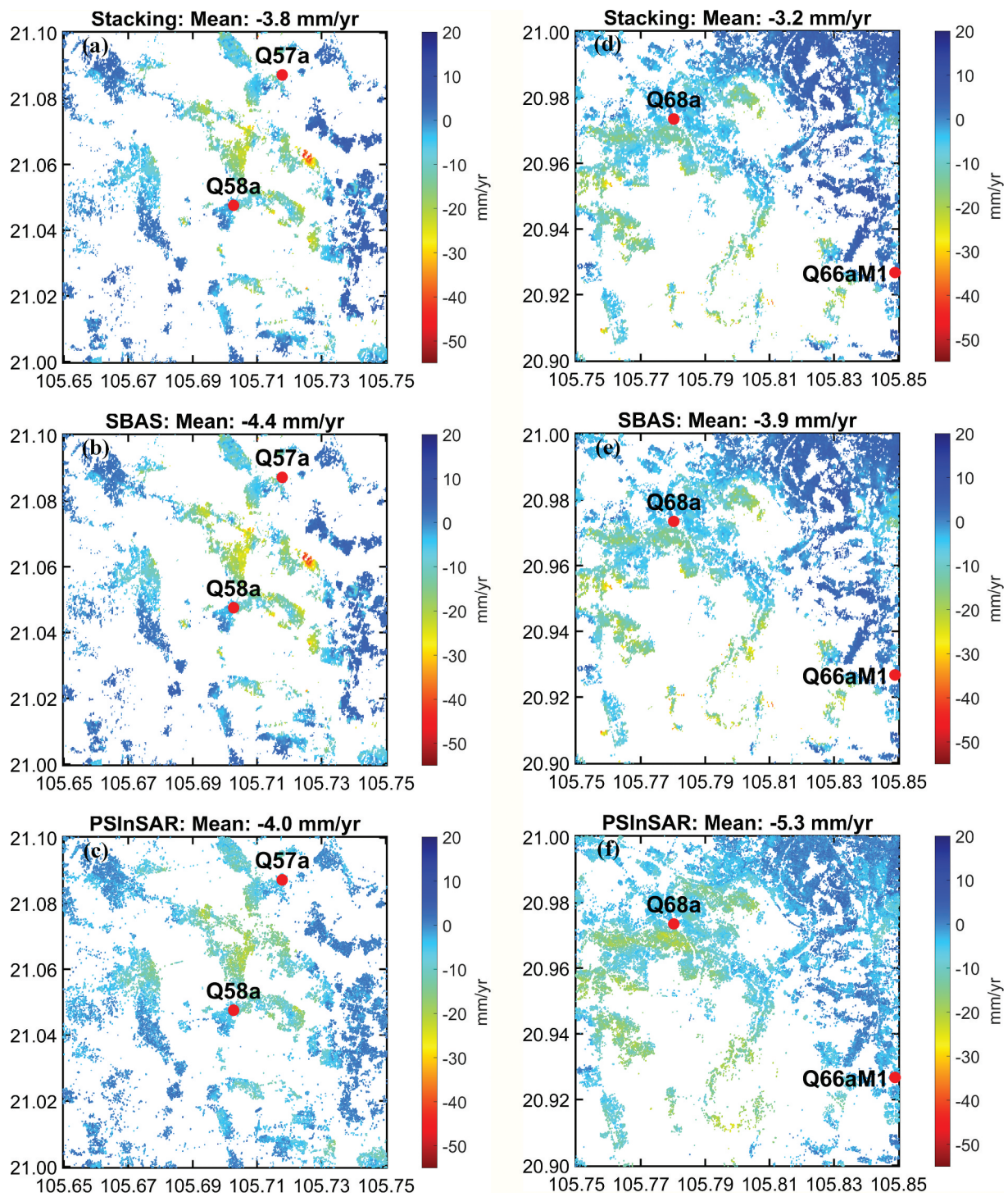


**Figure 6.** Maps of deformation rates zoomed in to  $0.1 \times 0.1$ -degree areas covering high rate subsiding bowls of Dan Phuong/Hoai Duc (a – c) and Ha Dong/Thanh Tri (d – f) derived from stacking, SBAS, and PSInSAR.

results indicate agreements in both spatial patterns and average rates between the three methods. In the case of Dan Phuong/Hoai Duc bowl, the mean rates from stacking, SBAS, and PSInSAR are  $-3.8$  mm/yr,  $-4.4$  mm/yr, and  $-4.0$  mm/yr, respectively, with

the center point being at  $[21.05^{\circ}\text{N}, 105.70^{\circ}\text{E}]$ , whilst those computed for the Ha Dong/Thanh Tri bowl are  $-3.2$  mm/yr,  $-3.9$  mm/yr, and  $-5.3$  mm/yr, respectively, with the center point being at  $[20.95^{\circ}\text{N}, 105.80^{\circ}\text{E}]$ .



### Validation against GPS-derived deformation

In this section, we compare the InSAR and GPS deformation time series at the two stations JNAV and PHUT shown in Figure 1. InSAR deformation is derived by averaging the time series from coherent pixels/scatterers located within areas limited by a circle of 100-m radius centered at each GPS station. It presents the surface movement in the line of sight (LOS) direction with respect to the mean displacement of the entire study area, whilst GPS-derived deformation is provided in a geocentric reference frame with both horizontal (i.e. in north and east directions) and vertical (i.e. in up direction) movements. GPS deformation at the JNAV station is therefore converted to the deformation in the LOS direction by (e.g. Fialko, Simons, and Agnew 2001; Hanssen 2001):

$$d_{LOS} = d_N \sin(\theta_{inc}) \sin(\alpha_h) - d_E \sin(\theta_{inc}) \cos(\alpha_h) + d_U \cos(\theta_{inc}) \quad 4$$

where  $d_{LOS}$  is the deformation in the LOS direction,  $d_N$ ,  $d_E$  and  $d_U$  are the GPS-derived deformation in north, east and up directions, respectively,  $\theta_{inc}$  and  $\alpha_h$  are the radar incidence angle and heading angle, respectively.

The InSAR time series cover a time period between 3 April 2016 and 13 March 2020 at a 12-day sampling interval, whilst the corresponding GPS time series at the JNAV station cover a time span from 7 January 2014 to 31 January 2018 with a daily interval. The common time between the two data is chosen (03/04/2016–31/01/2018) and the results are compared in Figure 7, which indicate high consistency between the PSInSAR- and SBAS-derived time series (cf. red and blue dots in Figure 7

(a)) with a correlation coefficient of 0.91 estimated at 95% confidence level (Figure 9(a)).

The InSAR and GPS deformation time series at this station show the seasonal cycle over the common time span, which were highly coherent within the 04/2016–2017 time span, but not beyond this period, i.e. after 2017. This is likely because GPS measurements reflect local deformation, which is probably the displacement of the GPS pillar or the building on which the GPS receiver was installed, whilst the InSAR measurements reflect the average movement of an area within a 100-m radius surrounding the GPS station, and the two objects likely did not move the same during the time period after 2017. As can be seen from Figure 7(b), the GPS deformation was dominated by the east component at the period later than 2017, which was larger than the other components, particularly the up displacement that got closer and closer to zero deformation, and this seems to be reflected by the local movement.

The GPS deformation time series at the PHUT station cover a time span between 24 February 2009 and 31 December 2018. Unfortunately, only the up component was provided through personal communication, thus it is converted to that in the LOS direction with an assumption that horizontal components are insignificant and thus negligible (Kampes 2006):

$$d_{LOS} = d_U \cos(\theta_{inc}) \quad 5$$

where  $d_{LOS}$  is the deformation in the LOS direction,  $\theta_{inc}$  is the radar incidence angle.

The common time between the InSAR and GPS datasets is chosen (03/04/2016–31/12/2018) then the deformation time series computed from those datasets at the PHUT station are compared and shown in Figure 8. High consistency between the

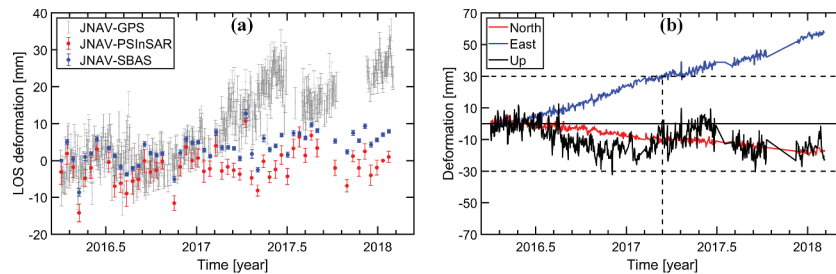


**Figure 7.** Comparison between InSAR- and GPS-derived deformation at the JNAV station: (a) the InSAR and GPS deformation time series in the LOS direction, (b) the GPS deformation time series in the north, east, up directions. Red, blue, and gray dots with error bars in the left panel indicate the PSInSAR-, SBAS-, and GPS-retrieved deformation time series, respectively. Black dashed lines in the right panel indicate the period when the GPS deformation in the east direction dominates the other components with their corresponding magnitudes.



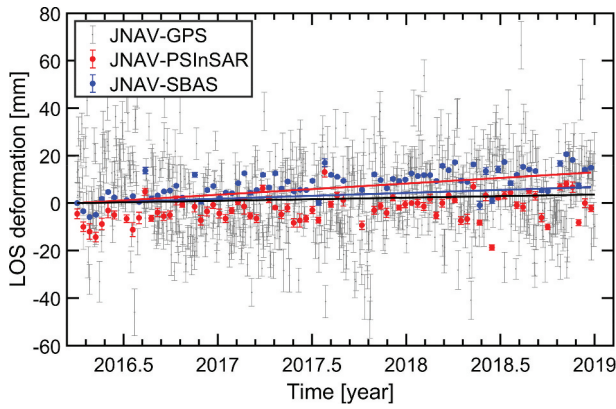


**Figure 8.** Comparison between InSAR- and GPS-derived deformation in the LOS direction at the PHUT station. Red, blue, and gray dots with error bars indicate the PSInSAR-, SBAS-, and GPS-retrieved deformation time series, respectively, with red, blue, and black lines representing their linear-fit trends.

PSInSAR- and SBAS-retrieved deformation time series is found (cf. red and blue dots in Figure 8), with a correlation coefficient of 0.80 estimated at a 95% confidence level (Figure 9(b)).

A seasonal cycle can be seen in Figure 8, particularly from the GPS time series, but this is vague. Instead, a linear trend is fit to those time series of which the results are depicted by red, blue, and black lines in Figure 8, indicating linear trends retrieved from PSInSAR, SBAS, and GPS, respectively. An agreement in the uplift trend is found from those results with annual rates of +4.9 mm/yr, +2.7 mm/yr, and +1.3 mm/yr derived from PSInSAR, SBAS, and GPS, respectively. We note that the InSAR derived rates indicate the relative surface movement of a 100-m area surrounding the GPS station with respect to the mean deformation

of the study area in the LOS direction, whilst that computed from the GPS measurements represents the movement of the GPS pillar in the geocentric reference frame. Furthermore, the GPS-retrieved rate is contributed by not only the vertical component but also the horizontal movement, which is not considered in this study due to its unavailability. Additionally, the difference in those retrieved rates falls within the accuracies of both InSAR and GPS, which are in the order of millimeters per year (Hooper et al. 2012).

Although the above assumption of insignificant horizontal movement has been adopted in many studies in the literature (e.g. Amelung et al. 1999; Chaussard et al. 2013, 2014; Kampes 2006; Parker, Filmer, and Featherstone 2017; Plattner et al. 2010), the computed results will encounter the influence caused by significantly horizontal movements.

Table 4 shows examples of this influence in terms of the error in computed deformation in the LOS direction, which is computed as the difference between Equations (4) and (5). These examples are computed using the incidence and heading angles equivalent to those in this study, which are 40 and  $-170$  degrees, respectively.

**Table 4.** Examples of errors in deformation in the LOS direction caused by significantly horizontal movements.

$d_N/d_E$ (mm)	$\theta_{inc}$ (degree)	$\theta_{inc}$ (degree)	$\Delta d_{LOS}$ (mm)
5	40	$-170$	3
10	40	$-170$	5
15	40	$-170$	8
20	40	$-170$	10
25	40	$-170$	13
30	40	$-170$	16

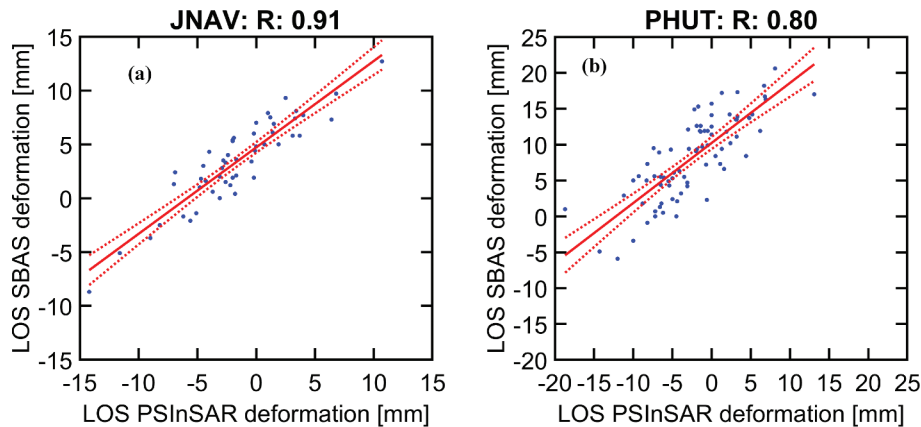


**Figure 9.** Correlation between the PSInSAR- and SBAS-retrieved deformation time series: (a) at the JNAV station, (b) at the PHUT station. Solid red lines indicate linear fit by a regression model with 95% confidence bounds represented by red dashed lines.

With the assumption that the movements in the north and east directions are equivalent, the errors are about half the magnitudes of north/east movements. In this case, the horizontal movements of GPS stations need to be considered as in Equation (4) to derive GPS deformation in the vertical. Alternatively, a combination of InSAR data in both ascending and descending directions can be adopted to quantify three-dimensional (i.e. horizontal and vertical) surface deformation (e.g. Fialko et al. 2005; Fialko, Simons, and Agnew 2001; Fuhrmann and Garthwaite 2019).

### ***The relationship between InSAR-derived deformation and groundwater depletion***

In Hanoi, groundwater over-exploitation has been documented as one of the main causes of surface subsidence, together with other factors, e.g. rapid urbanization or construction growth (e.g. Phi and Strokova 2015; Tran et al. 2015). During the last two decades, the annual drawdown of the groundwater level ranging from 0.3 m to 0.5 m led to surface subsidence up to 41 mm/yr (Vu and Tran 2018). Domestic water consumption in Hanoi is supplied mainly by groundwater extracted from the Pleistocene aquifer (qp) and the Holocene aquifer (qh) with a continuously increasing withdrawal. This increased from  $\sim 350,000 \text{ m}^3$  per day and  $\sim 200,000 \text{ m}^3$  per day extracted from the qp and the qh, respectively, before the 1990s to  $\sim 950,000 \text{ m}^3$  per day and  $\sim 350,000 \text{ m}^3$  per day by 2010. This remained stable since then thanks to assistance from a surface water treatment plant (Vu and Tran 2018).

The groundwater pumping is recently estimated at a rate of over one million  $\text{m}^3$  per day (Phi and Strokova 2015). Additionally, those factors are of a close relationship that promote each other. For instance, rapid urbanization in Hanoi, particularly after the administrative area expansion in 2008, has led to an increase in water demand for domestic, agricultural, and industrial consumptions. As shown in Section 4.1, two subsiding bowls of high rates – Dan Phuong/Hoai Duc and Ha Dong/Thanh Tri have been captured by InSAR. In this section, we measure the relationship between InSAR-derived deformation and groundwater level change in the Pleistocene aquifer at wells situated within or in close proximity to the two bowls (see Figure 4). At each well, SBAS and PSInSAR-derived

deformation is obtained by averaging the deformation time series from coherent pixels/scatterers bounded within a 100-m radius circle centered at the well location.

Figure 10 shows the InSAR-derived deformation time series and the changes in the hydraulic head at four wells located in Dan Phuong (Q57a), Hoai Duc (Q58a), Ha Dong (Q68a), and Thanh Tri (Q66aM1) districts, respectively. We note that the InSAR data are available at a 12-day sampling interval and between 4 March 2016 and 13 March 2020, whilst groundwater data were provided at a monthly temporal resolution between January 2005 and October 2018. Therefore, monthly-mean InSAR deformation is estimated by averaging the derived deformation over each month, then the two data are truncated to cover the common time between April 2016 and October 2018, which are shown in Figure 10 (right panel).

In general, we found that the three stations Q57a, Q58a, and Q68a experience surface subsidence at high rates due to their locations situated within the two subsiding bowls, but it is not the case for the station Q66aM1, which is situated outside the two bowls. Within the Dan Phuong/Hoai Duc subsiding bowl, the rates obtained from the SBAS and PSInSAR deformation time series at the Q57a borehole are  $-6.1 \text{ mm/yr}$  and  $-5.5 \text{ mm/yr}$ , respectively, whilst those at the Q58a borehole are  $-7.2 \text{ mm/yr}$  and  $-8.4 \text{ mm/yr}$ , respectively. These are consistent with the subsiding trend found in the hydraulic head changes in the two wells, which are  $-0.31 \text{ m/yr}$  at the Q57a station and  $-0.33 \text{ m/yr}$  at the Q58a station over the common time span between April 2016 and October 2018.

Q68a is the only well available located within the Ha Dong/Thanh Tri subsiding bowl with the SBAS- and PSInSAR-derived deformation rates of  $-6.7 \text{ mm/yr}$  and  $-7.4 \text{ mm/yr}$ , respectively. An agreed drawdown trend in the hydraulic head change can be found at the same station showing an annual rate of  $-0.93 \text{ m/yr}$ , which indicates the highest drawdown rate among the borehole stations. The three wells (i.e. Q57a, Q58a, and Q68a) within the subsiding bowls revealed that the localized subsidence is closely related to the exploitation of groundwater. We do not see a clear non-linear deformation or the correlation to the summer monsoon (i.e. precipitation) here, indicating that the ground deformation is dominant by an anthropogenic

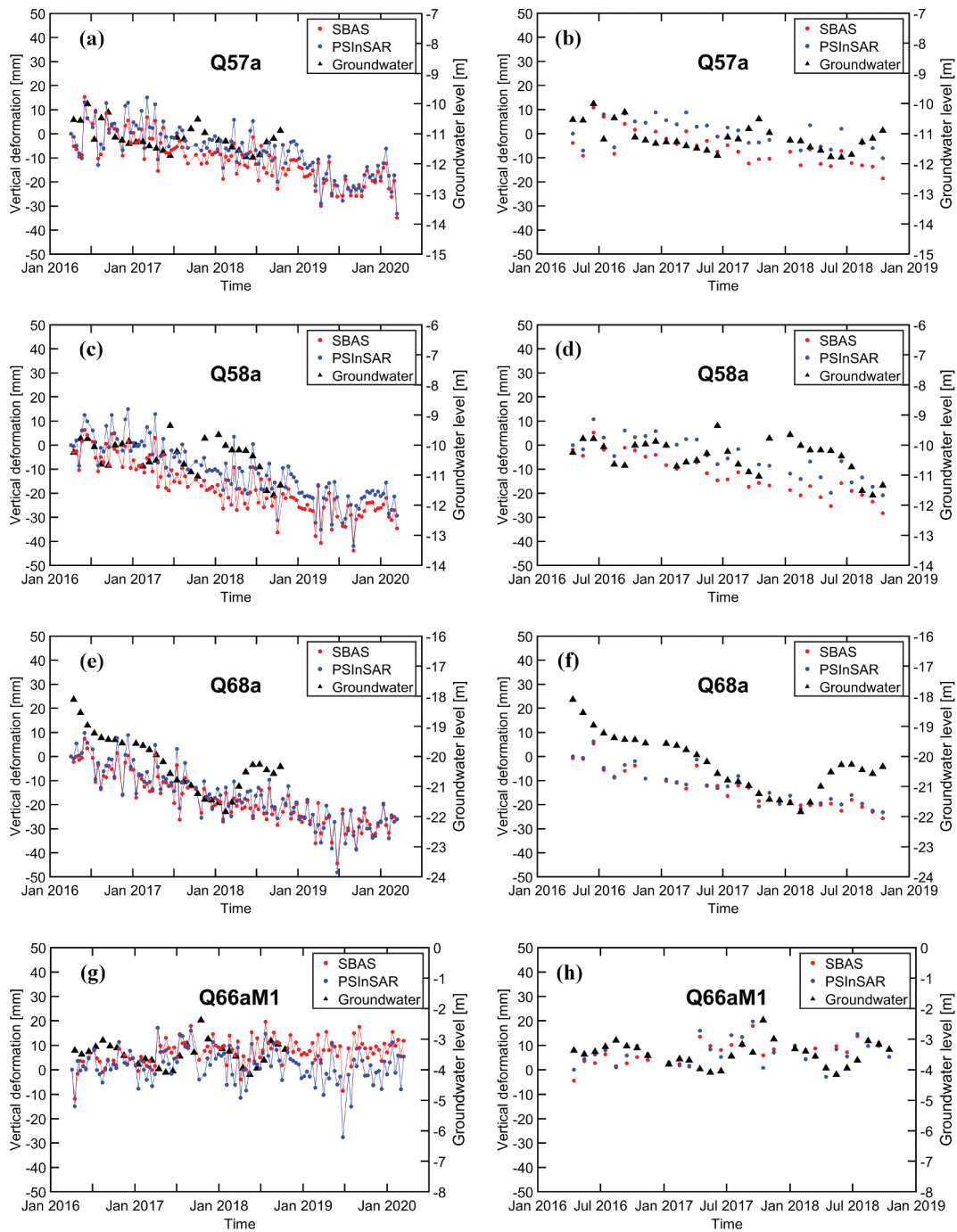


**Figure 10.** The PSInSAR- and SBAS-retrieved deformation time series in the LOS direction and groundwater level change at the wells located in: (a, b) Dan Phuong (Q57a), (c, d) Hoai Duc (Q58a), (e, f) Ha Dong (Q68a), and (g, h) Thanh Tri (Q66aM1). The InSAR deformation time series are shown at a 12-day sampling interval (left panel) and monthly-mean temporal resolution (right panel).

reason rather than the natural hydrologic process (Carlson et al. 2020; Hu, Lu, and Wang 2018). Although we observe some misfits of InSAR results and the tendency of water head measurements (e.g. between February and October 2018, Figure 10(f)), this may mainly be attributed to the delay effect from the

aquifer restoration and the pore pressure diffusion (Chaussard et al. 2017; Zhai et al. 2019).

At the Q66aM1 station located in the Thanh Tri area but outside the subsiding bowl (see Figure 4), small-magnitude deformation was observed by SBAS and PSInSAR with the annual rates of +1.8 mm/yr

and  $-0.4$  mm/yr, respectively. The two derived rates are in opposite trends (i.e. uplift and subsidence) likely resulted from low SNR (Bui, Featherstone, and Filmer 2020) and may indicate the limitation of InSAR to extract the deformation at a sub-millimeters level (Hooper et al. 2012). Considering the small fluctuation of deformation and the slight withdrawal of water head (i.e.  $-0.04$  m/yr), we argue that the surface in the vicinity of Q66aM1 is stable or slightly subsiding as revealed by PSInSAR results. We admit that the current number of wells may have some bias and cannot accurately reveal the spatial-temporal variation of groundwater, although it still gives out valuable information for the causative reason of deformation in the subsiding bowl. We suggest that more distributed wells can be deployed in the subsiding area, which can facilitate the numerical modeling and characterize the mechanism of deformation, and more in-situ geodetic measurements (i.e. GNSS and leveling) need to be conducted to validate the InSAR results.

## Conclusions

In this study, we have used Sentinel-1A SAR data to capture surface deformation over Hanoi, Vietnam for the period 2016 – 2020, which is also the most recent result of deformation detected by InSAR. 114 Sentinel-1A SAR images have been utilized in this study, which were processed by both the PSInSAR and SBAS methods. The deformation time series of two GPS stations have been adopted to validate InSAR results and groundwater level changes from four boreholes located within or in close proximity to areas of high-rate subsidence have been employed to measure the relationship between surface deformation and groundwater changes.

Results derived from SBAS and PSInSAR show their agreement in surface deformation rates in terms of the spatial patterns and rate statistics. The results indicated two subsiding bowls at high subsidence rates in Dan Phuong/Hoai Duc and Ha Dong/Thanh Tri, which are located to the south of the Red River, with a mean subsidence rate of approximately  $-5$  mm/yr. These were consistent with results from previous studies in the literature

though they reflected deformation at different time periods obtained from different SAR data.

The agreement between SBAS and PSInSAR indicates that the two methods can be applied to quantify surface deformation in Hanoi, in which nearly identical results can be obtained. However, they have their own advantages that should be considered in order to choose the optimal method. The advantage of PSInSAR is the network with fewer interferograms compared to that of SBAS as shown in this study, which may result in less computational burden and smaller disk storage requirement. In contrast, in the case of low SNR, SBAS is advantageous that more redundant interferograms are generated which may reduce the noise, and thus result in more precise deformation rates and trends detected.

The validation between the InSAR and GPS deformation time series generally showed high consistency though, at the JNAV station, the two data agreed well during the validated time up to 2017 only. The difference between the two data after that time can be attributable to the fact that GPS data reflected the local displacement of the GPS pillar or the building on which the GPS receiver was installed, whilst the InSAR measurements indicated the average movement of an area within a 100-m radius surrounding the GPS station, and the two objects likely did not move the same after 2017. At the other GPS station (PHUT), an agreement in the uplift trend was found at the rates of  $+4.9$  mm/yr,  $+2.7$  mm/yr, and  $+1.3$  mm/yr estimated from PSInSAR, SBAS, and GPS, respectively, in which the accuracies of both InSAR and GPS account for the difference between these rates.

Groundwater level changes and InSAR-derived deformation showed an agreement in the subsiding trend at four tested boreholes located within or in proximity to high-rate bowls. At two monitoring bores of Q57a and Q58a located within the Dan Phuong/Hoai Duc bowl, drawdown rates of the hydraulic head from April 2016 to October 2018 were recorded at about  $0.31$  m/yr with surface subsidence rates found between  $6$  and  $8$  mm/yr. The highest groundwater level change rate among these tested wells was found at the Q68a station located within the Ha Dong/Thanh Tri bowl, which was



estimated at a drawdown rate of ~0.9 m/yr during the same time period. The InSAR derived deformation rate estimated at this station was ~7 mm/yr.

## Acknowledgements

This research is funded by the Vietnam National Foundation for Science and Technology Development (NAFOSTED) under grant number 105.06–2017.320. The authors would like to acknowledge the European Space Agency for providing freely accessed Sentinel-1 data. We are also thankful to the Nevada Geodetic Laboratory and Vietnam Academy of Science and Technology for supplying GPS data and the Ministry of Natural Resources and Environment, Vietnam for providing borehole groundwater level data. We would also like to thank JPL/Caltech for providing open access to the ISCE and GIANt software as well as the software developers group at the University of Iceland, Delft University of Technology, and the University of Leeds for providing the StaMPS software package.

## Disclosure statement

The authors declare no conflict of interest.

## Funding

This research is funded by the Vietnam National Foundation for Science and Technology Development (NAFOSTED) under grant number [105.06–2017.320].

## ORCID

Luyen K. Bui  <http://orcid.org/0000-0003-1091-5573>  
 Phong V. V. Le  <http://orcid.org/0000-0001-5558-1023>  
 Phuong D. Dao  <http://orcid.org/0000-0002-3712-9022>  
 Nguyen Quoc Long  <http://orcid.org/0000-0002-4792-3684>  
 Hai V. Pham  <http://orcid.org/0000-0003-1016-4394>  
 Hong Ha Tran  <http://orcid.org/0000-0003-1130-386X>  
 Lei Xie  <http://orcid.org/0000-0003-0398-1476>

## References

- Agram, P. S., R. Jolivet, B. Riel, Y. N. Lin, M. Simons, E. Hetland, M. P. Doin, and C. Lasserre. 2013. "New Radar Interferometric Time Series analysis toolbox released." *Eos, Transactions, American Geophysical Union* 94 (7): 69–70. doi:10.1002/2013EO070001.
- Agram, P. S., R. Jolivet, and M. Simons (2012). "GIANt - the Generic InSAR analysis toolbox - user manual". Retrieved from [http://earthdef.caltech.edu/attachments/download/15/GIANt\\_doc.pdf](http://earthdef.caltech.edu/attachments/download/15/GIANt_doc.pdf)
- Amelung, F., D. L. Galloway, J. W. Bell, H. A. Zebker, and R. J. Laczniak. 1999. "Sensing the Ups and Downs of Las Vegas: InSAR Reveals structural control of land subsidence and aquifer-system deformation." *Geology* 27 (6): 483–486. doi:10.1130/0091-7613(1999)027<0483:stuado>2.3.CO;2.
- Bamler, R., and M. Eineder. 2005. "Accuracy of differential shift estimation by correlation and split-bandwidth interferometry for wideband and Delta-k SAR systems." *IEEE Geoscience and Remote Sensing Letters* 2 (2): 151–155. doi:10.1109/LGRS.2004.843203.
- Berardino, P., G. Fornaro, R. Lanari, and E. Sansosti. 2002. "A new algorithm for surface deformation monitoring based on small baseline Differential SAR Interferograms." *IEEE Transactions on Geoscience and Remote Sensing* 40 (11): 2375–2383. doi:10.1109/TGRS.2002.803792.
- Biggs, J., T. Wright, Z. Lu, and B. Parsons. 2007. "Multi-interferogram method for measuring interseismic deformation: Denali Fault, Alaska." *Geophysical Journal International* 170 (3): 1165–1179. doi:10.1111/j.1365-246X.2007.03415.x.
- Blewitt, G., W. C. Hammond, and C. Kreemer. 2018. "Harnessing the GPS data explosion for interdisciplinary science." *Eos* 99: 1–2. doi:10.1029/2018eo104623.
- Blewitt, G., C. Kreemer, W. C. Hammond, and J. Gazeaux. 2016. "MIDAS robust trend estimator for accurate GPS Station velocities without step detection." *Journal of Geophysical Research: Solid Earth* 121 (3): 2054–2068. doi:10.1002/2015JB012552.
- Bonforte, A., and F. Guglielmino. 2015. "Very shallow dyke intrusion and potential slope failure imaged by ground deformation: The 28 December 2014 Eruption on Mount Etna." *Geophysical Research Letters* 42 (8): 2727–2733. doi:10.1002/2015GL063462.
- Bui, D. D., A. Kawamura, T. N. Tong, H. Amaguchi, N. Nakagawa, and Y. Iseri. 2011. "Identification of aquifer system in the whole red river delta, Vietnam." *Geosciences Journal* 15 (3): 323–338. doi:10.1007/s12303-011-0024-x.
- Bui, L. K., W. E. Featherstone, and M. S. Filmer. 2020. "Disruptive influences of residual noise, network configuration and data gaps on InSAR-derived land motion rates using the SBAS Technique." *Remote Sensing of Environment* 247: 111941. doi:10.1016/j.rse.2020.111941.
- Carlson, G., M. Shirzaei, S. Werth, G. Zhai, and C. Ojha. 2020. "Seasonal and long-term groundwater unloading in the central valley modifies crustal stress." *Journal of Geophysical Research: Solid Earth* 125(1). Article e2019JB018490. doi:10.1029/2019JB018490.
- Cavalié, O., M. P. Doin, C. Lasserre, and P. Briole. 2007. "Ground motion measurement in the lake mead area, nevada, by differential synthetic aperture Radar Interferometry Time Series Analysis: Probing the lithosphere rheological structure." *Journal of Geophysical Research: Solid Earth* 112 (B3): 1–18. doi:10.1029/2006JB004344. Article B03403.
- Cavalié, O., C. Lasserre, M.-P. Doin, G. Peltzer, J. Sun, X. Xu, and Z.-K. Shen. 2008. "Measurement of interseismic strain across the haiyuan fault (Gansu, China), by InSAR." *Earth and Planetary Science Letters* 275 (3–4): 246–257. doi:10.1016/j.epsl.2008.07.057.
- Chaussard, E., F. Amelung, H. Abidin, and S. H. Hong. 2013. "Sinking cities in Indonesia: ALOS PALSAR detects rapid

- subsidence due to groundwater and gas extraction." *Remote Sensing of Environment* 128: 150–161. doi:10.1016/j.rse.2012.10.015.
- Chaussard, E., P. Milillo, R. Bürgmann, D. Perissin, E. J. Fielding, and B. Baker. 2017. "Remote sensing of ground deformation for monitoring groundwater management practices: Application to the Santa Clara Valley during the 2012–2015 California Drought." *Journal of Geophysical Research: Solid Earth* 122 (10): 8566–8582. doi:10.1002/2017JB014676.
- Chaussard, E., S. Wdowinski, E. Cabral-Cano, and F. Amelung. 2014. "Land subsidence in central Mexico detected by ALOS InSAR Time-series." *Remote Sensing of Environment* 140: 94–106. doi:10.1016/j.rse.2013.08.038.
- Chen, C. W., and H. A. Zebker. 2000. "Network approaches to two-dimensional phase unwrapping: Intractability and two new algorithms." *Journal of the Optical Society of America A: Optics and Image Science, and Vision* 17 (3): 401–414. doi:10.1364/JOSAA.17.000401.
- Colesanti, C., A. Ferretti, F. Novali, C. Prati, and F. Rocca. 2003. "SAR monitoring of progressive and seasonal ground deformation using the permanent scatterers technique." *IEEE Transactions on Geoscience and Remote Sensing* 41 (7): 1685–1701. doi:10.1109/TGRS.2003.813278.
- Costantini, M. T. 1998. "A novel phase unwrapping method based on network programming." *IEEE Transactions on Geoscience and Remote Sensing* 36 (3): 813–821. doi:10.1109/36.673674.
- Crosetto, M., O. Monserrat, M. Cuevas-González, N. Devanthery, and B. Crippa. 2016. "Persistent scatterer interferometry: A review." *ISPRS Journal of Photogrammetry and Remote Sensing* 115: 78–89. doi:10.1016/j.isprsjprs.2015.10.011.
- Dang, V., C. Doubré, C. Weber, N. Gourmelen, and F. Masson. 2014. "Recent land subsidence caused by the rapid urban development in the Hanoi Region (Vietnam) using ALOS InSAR data." *Nat. Hazards Earth Syst. Sci* 14: 657–674. doi:10.5194/nhess-14-657-2014.
- De Zan, F., and A. M. Guarnieri. 2006. "TOPSAR: Terrain Observation by Progressive Scans." *IEEE Transactions on Geoscience and Remote Sensing* 44 (9): 2352–2360. doi:10.1109/TGRS.2006.873853. Article 1677745.
- Doin, M. P., C. Lasserre, G. Peltzer, O. Cavalié, and C. Doubré. 2009. "Corrections of stratified tropospheric delays in SAR interferometry: Validation with global atmospheric models." *Journal of Applied Geophysics* 69 (1): 35–50. doi:10.1016/j.jappgeo.2009.03.010.
- Eineder, M., M. Hubig, and B. Milcke (1998). "Unwrapping large interferograms using the minimum cost flow algorithm". *Proceedings of the IGARSS '98 Sensing and Managing the Environment International Geoscience and Remote Sensing Symposium (IGARSS)*, Seattle, WA, USA, 83–87. doi:10.1109/igarss.1998.702806.
- Emardson, T. R., M. Simons, and F. H. Webb. 2003. "Neutral atmospheric delay in interferometric synthetic aperture radar applications: Statistical description and mitigation." *Journal of Geophysical Research B: Solid Earth* 108 (B5): ETG 4–1–4–8. doi:10.1029/2002JB001781.
- Farr, T. G., and M. Kobrick. 2000. "Shuttle radar topography mission produces a wealth of data." *Eos* 81 (48): 583–585. doi:10.1029/EO081i048p00583.
- Fattahi, H., P. Agram, and M. Simons. 2017. "A network-based enhanced spectral diversity approach for TOPS time-series analysis." *IEEE Transactions on Geoscience and Remote Sensing* 55 (2): 777–786. doi:10.1109/TGRS.2016.2614925. Article 7637021.
- Ferretti, A., C. Prati, and F. Rocca. 2001. "Permanent scatterers in SAR interferometry." *IEEE Transactions on Geoscience and Remote Sensing* 39 (1): 8–20. doi:10.1109/36.898661.
- Fialko, Y., D. Sandwell, M. Simons, and P. Rosen. 2005. "Three-dimensional deformation caused by the Bam, Iran, Earthquake and the origin of shallow slip deficit." *Nature* 435 (7040): 295–299. doi:10.1038/nature03425.
- Fialko, Y., M. Simons, and D. Agnew. 2001. "The complete (3-D) surface displacement field in the epicentral area of the 1999 Mw 7.1 Hector Mine Earthquake, California, from Space Geodetic Observations." *Geophysical Research Letters* 28 (16): 3063–3066. doi:10.1029/2001GL013174.
- Fuhrmann, T., and M. C. Garthwaite. 2019. "Resolving three-dimensional surface motion with InSAR: Constraints from multi-geometry data fusion." *Remote Sensing* 11 (3): 241. doi:10.3390/rs11030241. Article 241.
- Goldstein, R. M., and C. L. Werner. 1998. "Radar interferogram filtering for geophysical applications." *Geophysical Research Letters* 25 (21): 4035–4038. doi:10.1029/1998gl900033.
- González, P. J., M. Bagnardi, A. Hooper, Y. Larsen, P. Marinkovic, S. V. Samsonov, and T. J. Wright. 2015. "The 2014–2015 eruption of Fogo volcano: Geodetic modeling of Sentinel-1 TOPS interferometry." *Geophysical Research Letters* 42 (21): 9239–9246. doi:10.1002/2015GL066003.
- Grandin, R., E. Klein, M. Métois, and C. Vigny. 2016. "Three-dimensional displacement field of the 2015 Mw8.3 Illapel Earthquake (Chile) from across- and along-track Sentinel-1 TOPS Interferometry." *Geophysical Research Letters* 43 (6): 2552–2561. doi:10.1002/2016GL067954.
- Hammond, W. C., G. Blewitt, and C. Kreemer. 2016. "GPS imaging of vertical land motion in California and Nevada: Implications for Sierra Nevada uplift." *Journal of Geophysical Research: Solid Earth* 121 (10): 7681–7703. doi:10.1002/2016JB013458.
- Hanssen, R. (2001). "Radar interferometry: Data interpretation and error analysis". In *Remote Sensing and Digital Image Processing* (Vol.2, pp. XVIII, 308). Springer Netherlands. doi:10.1007/0-306-47633-9.
- Hetland, E. A., P. Musé, M. Simons, Y. N. Lin, P. S. Agram, and C. J. DiCaprio. 2012. "Multiscale InSAR time series (mints) analysis of surface deformation." *Journal of Geophysical Research: Solid Earth* 117 (B2): B02404. doi:10.1029/2011JB008731.
- Ho, D. M. T., C. Q. Tran, Q. N. Pham, T. T. Dang, D. A. Nguyen, I. El-Moussawi, and T. T. Le. 2019. "Measuring ground subsidence in Hanoi through the radar interferometry technique using TerraSAR-X and COSMO-SkyMed data." *IEEE Journal of Selected Topics in Applied Earth Observations and Remote Sensing* 12 (10): 3874–3884. doi:10.1109/JSTARS.2019.2937398. Article 8827271.

- Hooper, A., D. P. S. Bekaert, K. Spaans, and M. Arkan. 2012. "Recent advances in SAR interferometry time series analysis for measuring crustal deformation." *Tectonophysics* 514–517: 1–13. doi:10.1016/j.tecto.2011.10.013.
- Hooper, A., and H. A. Zebker. 2007. "Phase unwrapping in three dimensions with application to INSAR time series." *Journal of the Optical Society of America A: Optics and Image Science, and Vision* 24 (9): 2737–2747. doi:10.1364/JOSAA.24.002737.
- Hooper, A., H. A. Zebker, P. Segall, and B. Kampes. 2004. "A new method for measuring deformation on volcanoes and other natural terrains using InSAR persistent scatterers." *Geophysical Research Letters* 31 (23): L23611. doi:10.1029/2004GL021737.
- Hu, X., Z. Lu, and T. Wang. 2018. "Characterization of hydrogeological properties in Salt Lake Valley, Utah, using InSAR." *Journal of Geophysical Research: Earth Surface* 123 (6): 1257–1271. doi:10.1029/2017JF004497.
- Jolivet, R., R. Grandin, C. Lasserre, M. P. Doin, and G. Peltzer. 2011. "Systematic InSAR tropospheric phase delay corrections from global meteorological reanalysis data." *Geophysical Research Letters* 38 (17): L17311. doi:10.1029/2011GL048757. Article L17311.
- Jolivet, R., C. Lasserre, M. P. Doin, S. Guillaso, G. Peltzer, R. Dailu, J. Sun, Z. K. Shen, and X. Xu. 2012. "Shallow creep on the haiyuan fault (Gansu, China) revealed by SAR interferometry." *Journal of Geophysical Research: Solid Earth* 117 (B6): B06401. doi:10.1029/2011JB008732.
- Kampes, B. M. 2006. *Radar Interferometry: Persistent Scatterer Technique*. 1–213 Vol. 12 Book Springer. doi:10.1007/978-1-4020-4723-7.
- Lavecchia, G., R. Castaldo, R. de Nardis, V. De Novellis, F. Ferrarini, S. Pepe, F. Brozzetti, et al. 2016. "Ground deformation and source geometry of the 24 August 2016 amatrice earthquake (Central Italy) investigated through analytical and numerical modeling of DInSAR measurements and structural-geological data." *Geophysical Research Letters* 43 (24): 12,389–312,398. doi:10.1002/2016GL071723.
- Le, M. H., K. Feigl, F. Masson, C. C. Duong, A. Bourdillon, P. L. Duchesne, T. C. Nguyen, T. H. Nguyen, N. N. Tran, and L. T. Hoang. 2014. "Recent crustal motion in vietnam and in the southeast asia region by continuous GPS data." *Vietnam Journal of Earth Sciences* 32 (3): 249–260. doi:10.15625/0866-7187/32/3/1026.
- Le, M. H., L. T. Tran, C. Amory-Mazaudier, R. Fleury, A. Bourdillon, J. Hu, H. T. Vu, T. C. Nguyen, T. T. Le, and T. H. Nguyen. 2016a. "Continuous GPS network in Vietnam and results of study on the total electron content in the South East Asian Region." *Vietnam Journal of Earth Sciences* 38 (2): 153–165. doi:10.15625/0866-7187/38/2/8598.
- Le, T. S., C. P. Chang, X. T. Nguyen, and A. Yokhka. 2016b. "TerraSAR-X Data for High-precision Land subsidence monitoring: A case study in the historical centre of Hanoi, Vietnam." *Remote Sensing* 8 (4): 338. doi:10.3390/rs8040338. Article 338.
- Lin, Y. N. N., M. Simons, E. A. Hetland, P. Muse, and C. DiCaprio. 2010. "A multiscale approach to estimating topographically correlated propagation delays in Radar Interferograms." *Geochemistry, Geophysics, Geosystems* 11 (9): 1–17. doi:10.1029/2010GC003228. Article Q09002.
- López-Quiroz, P., M.-P. Doin, F. Tupin, P. Briole, and J.-M. Nicolas. 2009. "Time series analysis of Mexico City subsidence constrained by Radar Interferometry." *Journal of Applied Geophysics* 69 (1): 1–15. doi:10.1016/j.jappgeo.2009.02.006.
- Luo, P., D. Mu, H. Xue, T. Ngo-Duc, K. Dang-Dinh, K. Takara, D. Nover, and G. Schladow. 2018. "Flood inundation assessment for the Hanoi central Area, Vietnam under historical and extreme rainfall conditions." *Scientific Reports* 8(1). Article 12623. doi:10.1038/s41598-018-30024-5.
- Lyons, S., and D. Sandwell. 2003. "Fault creep along the Southern San Andreas from interferometric synthetic Aperture Radar, Permanent Scatterers, and Stacking." *Journal of Geophysical Research: Solid Earth* 108 (B1): ETG 11–11–11–24. doi:10.1029/2002JB001831.
- Motagh, M., R. Shamshiri, M. Haghshenas Haghghi, H. U. Wetzel, B. Akbari, H. Nahavandchi, S. Roessner, and S. Arabi. 2017. "Quantifying groundwater exploitation induced subsidence in the Rafsanjan Plain, Southeastern Iran, using InSAR time-series and in situ measurements." *Engineering Geology* 218: 134–151. doi:10.1016/j.enggeo.2017.01.011.
- Nguyen, A. K., Y. A. Liou, M. H. Li, A. Van Tran, and B. Van Do (2017). "Groundwater arsenic contamination and land subsidence in Hanoi City", Vietnam. International Geoscience and Remote Sensing Symposium (IGARSS), 5602–5605. doi:10.1109/IGARSS.2017.8128275.
- Nguyen, T. H. T., V. T. Tran, Q. T. Bui, Q. H. Man, and T. V. Walter. 2016. "Socio-economic effects of agricultural land conversion for urban development: Case Study of Hanoi, Vietnam." *Land Use Policy* 54: 583–592. doi:10.1016/j.landusepol.2016.02.032.
- Nguyen, T. Q., and D. C. Helm. 1995. *Land Subsidence Due to Groundwater Withdrawal in Hanoi*, 55–60. Vietnam: IAHS-AISH Publication.
- Parker, A. L., M. S. Filmer, and W. E. Featherstone. 2017. "First results from Sentinel-1A InSAR over Australia: Application to the Perth Basin." *Remote Sensing* 9 (3): 299. doi:10.3390/rs9030299. Article 299.
- Pepe, A., and R. Lanari. 2006. "On the extension of the minimum cost flow algorithm for Phase Unwrapping of Multitemporal Differential SAR Interferograms." *IEEE Transactions on Geoscience and Remote Sensing* 44 (9): 2374–2383. doi:10.1109/TGRS.2006.873207. Article 1677747.
- Pham, G. H., H. T. Vu, H. D. Nguyen, A. H. T. Nguyen, and M. N. Nguyen. 2018. "Land subsidence prediction for a new urban mass rapid transit line in Hanoi." *Underground Space*. doi:10.1016/j.undsp.2018.11.002.
- Phi, T. H., and L. A. Strokova. 2015. "Prediction maps of land subsidence caused by groundwater exploitation in Hanoi, Vietnam." *Resource-Efficient Technologies* 1 (2): 80–89. j.refffit.2015.09.001.
- Plattner, C., S. Wdowinski, T. H. Dixon, and J. Biggs. 2010. "Surface subsidence induced by the Crandall Canyon Mine (Utah) Collapse: InSAR Observations and Elasto-plastic Modelling." *Geophysical Journal International* 183 (3): 1089–1096. doi:10.1111/j.1365-246X.2010.04803.x.
- Prats-Iraola, P., R. Scheiber, L. Marotti, S. Wollstadt, and A. Reigber. 2012. "TOPS Interferometry with terraSAR-X." *IEEE Transactions on Geoscience and Remote Sensing* 50 (8):

- 3179–3188. doi:10.1109/TGRS.2011.2178247. Article 6130599.
- Pritchard, M. E., C. Ji, and M. Simons. 2006. "Distribution of slip from 11 Mw > 6 Earthquakes in the Northern Chile Subduction Zone." *Journal of Geophysical Research: Solid Earth* 111(10). Article B10302. doi:10.1029/2005JB004013.
- Raucoules, D., and C. Carnec (2000). "DEM derivation and subsidence detection on Hanoi from ERS SAR Interferometry". European Space Agency, (Special Publication) ESA SP, 553–558. <https://www.scopus.com/inward/record.uri?eid=2-s2.0-0347051451&partnerID=40&md5=279c7184289804b6da2ce43dc67b40e6>
- Rosen, P. A., E. M. Gurrola, P. Agram, J. Cohen, M. Lavalle, B. V. Riel, H. Fattahi, M. A. G. Aivazis, M. Simons, and S. M. Buckley. (2018). "The InSAR scientific computing environment 3.0: A Flexible Framework for NISAR Operational and User-led Science Processing". International Geoscience and Remote Sensing Symposium (IGARSS), 4897–4900. doi:10.1109/IGARSS.2018.8517504.
- Rosen, P. A., E. M. Gurrola, G. F. Sacco, and H. A. Zebker. (2012). "The InSAR scientific computing environment. Synthetic Aperture Radar." 2012.EUSAR. 9th European Conference on Synthetic Aperture Radar, 730–733.
- Rosen, P. A., S. Hensley, I. R. Joughin, F. Li, S. N. Madsen, E. Rodriguez, and R. M. Goldstein. 2000. "Synthetic Aperture Radar Interferometry." *Proceedings of the IEEE* 88 (3) (March): 333–382. doi:10.1109/5.838084.
- Sansosti, E., P. Berardino, M. Manunta, F. Serafino, and G. Fornaro. 2006. "Geometrical SAR Image Registration." *IEEE Transactions on Geoscience and Remote Sensing* 44 (10): 2861–2870. doi:10.1109/TGRS.2006.875787. Article 1704979.
- Saraswat, C., P. Kumar, and B. K. Mishra. 2016. "Assessment of stormwater runoff management practices and governance under climate change and urbanization: An analysis of Bangkok, Hanoi and Tokyo." *Environmental Science & Policy* 64: 101–117. doi:10.1016/j.envsci.2016.06.018.
- Schmidt, D. A., and R. Bürgmann. 2003. "Time-dependent Land Uplift and Subsidence in the Santa Clara Valley, California, from a large interferometric synthetic Aperture Radar Data Set." *Journal of Geophysical Research: Solid Earth* 108 (B9): B9. doi:10.1029/2002JB002267.
- Schramm, S. 2016. "Flooding the Sanitary city: Planning discourse and the materiality of Urban Sanitation in Hanoi." *City* 20 (1): 32–51. doi:10.1080/13604813.2015.1125717.
- Shanker, P., F. Casu, H. A. Zebker, and R. Lanari. 2011. "Comparison of persistent scatterers and small baseline time-series InSAR Results: A Case Study of the San Francisco Bay Area." *IEEE Geoscience and Remote Sensing Letters* 8 (4): 592–596. doi:10.1109/LGRS.2010.2095829. Article 5692806.
- Simons, M., and P. A. Rosen. 2015. "Interferometric Synthetic Aperture Radar Geodesy". In *Treatise on Geophysics: Second Edition*, edited by G. Schubert, 339–385. 2nd ed. Vol. 3. Elsevier. doi:10.1016/B978-0-444-53802-4.00061-0.
- Smith, B., and D. Sandwell. 2003. "Accuracy and resolution of shuttle radar topography mission data." *Geophysical Research Letters* 30 (9): 20–21–20–24. doi:10.1029/2002GL016643.
- Sowter, A., M. Bin Che Amat, F. Cigna, S. Marsh, A. Athab, and L. Alshammari. 2016. "Mexico City land subsidence in 2014–2015 with Sentinel-1 IW TOPS: Results using the intermittent SBAS (ISBAS) technique." *International Journal of Applied Earth Observation and Geoinformation* 52: 230–242. doi:10.1016/j.jag.2016.06.015.
- Torres, R., P. Snoeij, D. Geudtner, D. Bibby, M. Davidson, E. Attema, P. Potin, et al. 2012. "GMES Sentinel-1 Mission." *Remote Sensing of Environment* 120: 9–24. doi:10.1016/j.rse.2011.05.028.
- Tran, A. V., S. Masumoto, V. Raghavan, and K. Shiono. 2007. "Spatial distribution of subsidence in Hanoi detected by JERS-1 SAR interferometry." *Geoinformatics* 18 (1): 3–13. doi:10.6010/geoinformatics.18.3.
- Tran, C. Q., D. M. T. Ho, T. V. Le, and T. T. Le. (2015). "Ground subsidence monitoring in Vietnam by multi-temporal InSAR technique". *International Geoscience and Remote Sensing Symposium (IGARSS)* 3540–3543. doi:10.1109/IGARSS.2015.7326585.
- Trinh, T. M., and D. G. Fredlund. 2000. "Modelling subsidence in the Hanoi city area, Vietnam." *Canadian Geotechnical Journal* 37 (3): 621–637. doi:10.1139/t99-126.
- Tuladhar, R., N. N. H. Cuong, and F. Yamazaki. 2004. *Seismic Microzonation of Hanoi, Vietnam Using Microtremor Observations. 13th World Conference on Earthquake Engineering*. Vancouver, BC, Canada.
- Usai, S. 2003. "A least squares database approach for SAR interferometric data." *IEEE Transactions on Geoscience and Remote Sensing* 41 (4): 753–760. doi:10.1109/TGRS.2003.810675.
- Vu, T. T., and N. V. T. Tran. 2018. "Assessment of urbanization impact on groundwater resources in Hanoi, Vietnam." *Journal of Environmental Management* 227: 107–116. doi:10.1016/j.jenvman.2018.08.087.
- Werner, C., U. Wegmüller, T. Strozzi, and A. Wiesmann (2003). "Interferometric point target analysis for deformation mapping". International Geoscience and Remote Sensing Symposium (IGARSS), 4362–4364.
- Yague-Martinez, N., P. Prats-Iraola, F. R. Gonzalez, R. Brcic, R. Shau, D. Geudtner, M. Eineder, and R. Bamler. 2016. "Interferometric processing of sentinel-1 TOPS data." *IEEE Transactions on Geoscience and Remote Sensing* 54 (4): 2220–2234. doi:10.1109/TGRS.2015.2497902. Article 7390052.
- Zebker, H. A., and J. Villasenor. 1992. "Decorrelation in interferometric radar echoes." *IEEE Transactions on Geoscience and Remote Sensing* 30 (5): 950–959. doi:10.1109/36.175330.
- Zhai, G., M. Shirzaei, M. Manga, and X. Chen. 2019. "Pore-pressure diffusion, enhanced by poroelastic stresses, controls induced seismicity in Oklahoma." *Proceedings of the National Academy of Sciences of the United States of America* 116 (33): 16228–16233. doi:10.1073/pnas.1819225116.